Dalton
Transactions

PAPER

View Article Online
View Journal

Cite this: DOI: 10.1039/c5dt01805f

Hierarchical nanospheres based on Pd nanoparticles dispersed on carbon coated magnetite cores with a mesoporous ceria shell: a highly integrated multifunctional catalyst†

Yinle Li, Zhuqing Zhang, Jianfeng Shen and Mingxin Ye*

Received 14th May 2015,
Accepted 18th August 2015

DOI: 10.1039/c5dt01805f

www.rsc.org/dalton

The design and fabrication of core–shell nanostructures with steerable morphologies and tailored performances have aroused abundant scientific studies for organic transformations. We here report the preparation of multifunctional and highly efficient core–shell microspheres, which bear a carbon-protected magnetic Fe_3O_4 core, a transition layer of active Pd nanoparticles (NPs) and an outer shell of mesoporous CeO_2 ($m$$CeO_2$). The composition and structure of the as-prepared Fe_3O_4@C–Pd@$m$$CeO_2$ were thoroughly characterized by X-ray photoelectron spectroscopy, transmission electron microscopy, scanning electron microscopy, X-ray diffraction, Fourier-transform infrared spectroscopy and Brunauer–Emmett–Teller measurements. The well-designed microspheres have high dispersibility, convenient magnetic separability and good reusability as heterogeneous nanoreactors due to their unique structure. We illustrate the high efficiency of these nanocomposites in mediating the Suzuki–Miyaura cross-coupling reaction and the reduction reaction of 4-nitrophenol (4-NP). The enhanced catalytic activity can be attributed to the synergistic effect between the CeO_2 nanoparticles and noble metal NPs. A mechanism was further proposed to explain the improved catalytic activity. This peculiar core–shell nanostructure renders the nanospheres to be an approachable and attractive catalyst system for various catalytic organic industrial processes.

Introduction

Owing to the extraordinary advantages of their unique optical, electrochemical and catalytic properties, noble metal NPs have become promising materials for underlying applications in various fields.[1–5] In particular, with the property of the high surface-to-volume ratio and the superiority of incorporating various homogeneous and heterogeneous catalysis,[6] the employment of noble metal nanoparticles (such as Pd,[7] Au,[8] Pt,[9] and Ag[10]) in catalytic reactions has aroused enormous scientific research. However, naked noble metal NPs tend to aggregate and sinter, leading to the loss of catalytic activity under reaction conditions. Therefore, solving this predicament and promoting environmental consciousness are imperative parts of these studies,[11–14] and also enhancing efficiency of the catalysts in chemical reactions under a friendly condition with recyclable reuse is equally important. Loading noble metal NPs onto the special surface of supports is one of the best approaches to boost the efficiency and recyclability of the catalysts.[15,16]

Currently, the introduction of magnetic NPs in various solid matrices permits the assembly of well-known programs for catalyst heterogenization with magnetic separation.[17,18] Magnetite is an ideal support that is easy to prepare and it has a proper active surface for the immobilization of metals and ligands, which can be isolated by magnetic decantation after the completion of a reaction, thus making it a better sustainable catalyst.[19–21] In the last few years, the magnetic core–shell nanostructure,[22,23] a special type of universal functional composite with a distinct microstructure, has shown a great application for loading noble metal NPs.[24–29] Generally, silica or carbon as a protecting shell is employed to coat the magnetic particles to obtain the shape of core–shell nanostructured (Fe_3O_4@SiO_2 or Fe_3O_4@C).[30–33] Moreover, a silica or carbon shell can prevent the magnetic particles from losing their magnetic properties in acidic environments and provide numerous functionalized groups for further modification. Several noble metal NPs dispersed on the surface of Fe_3O_4@SiO_2 or Fe_3O_4@C core–shell nanostructures have been reported in an attempt to achieve easy separation and recyclable catalytic processes including methanol oxidation,[34] Fenton-like catalysis,[35] hydrogenation[36] and cross-coupling reactions.[31] However, the active metal NPs on the surface of core–shell nanostructure directly exposed in reaction condition can be easily leached.

Center of Special Materials and Technology, Fudan University, Shanghai 200433, China. E-mail: meye@fudan.edu.cn

† Electronic supplementary information (ESI) available. See DOI: 10.1039/c5dt01805f

The novel mesoporous "shell-in-shell" hierarchical structures are composed of a mesoporous outermost shell and protected magnetic inside core–shell structure with the ultrafine active metal NPs distributed on the internal and external surface that endows the nanocatalyst with high stability, reducing the leaching of active metal NPs, and an independent cavity is formed by two shells.[36,37] Zhao *et al.*[38] synthesized multicomponent and multifunctional Fe_3O_4@C–Pd@*m*SiO_2 hierarchical "shell-in-shell" structures for the Suzuki–Miyaura coupling reaction. According to our investigation, there are only a few reports about the assembling of magnetic core–shell nanocatalyst with active hierarchical structures, because the precise control of the morphology, structure and assembly process of each section is always troublesome.

Herein, we report novel, well-defined hierarchical "shell-in-shell" structures of Fe_3O_4@C–Pd@*m*CeO_2 consisting of a core of carbon-protected magnetite particles, a transition layer of confined catalytic Pd nanoparticles, and an outer shell of mesoporous CeO_2. The outermost CeO_2 shell can not only prevent active Pd NPs from aggregating, sintering and leaching, but also improve the catalytic activity due to a strong synergistic effect between the CeO_2 nanoparticles and noble metal NPs.[39] The well-designed Fe_3O_4@C–Pd@*m*CeO_2 hierarchical core–shell structures possess the advantages of large magnetization, being highly open mesoporous and they disperse well in water. The multifunctional catalytic activities were systematically tested for catalyzing the Suzuki–Miyaura cross-coupling reaction and the reduction reaction of 4-NP. The studies reveal that the CeO_2 nanoparticles and noble metal NPs exhibit excellent synergetic catalytic performance and the good reusability of the system by the magnetic separation for both the reactions. Our results, therefore afford a general way based on a hierarchical core–shell structure for the preparation of high performance magnetic catalysts loaded with noble metal NPs, which will be a very useful tool for various catalytic organic industry processes.

Experimental

Materials

Ferric chloride hexahydrate ($FeCl_3 \cdot 6H_2O$), trisodium citrate, palladium(II) chloride ($PdCl_2$), sodium acetate (NaAc), ethylene glycol (EG), glucose, cerium(III) nitrate hexahydrate ($Ce(NO_3)_3 \cdot 6H_2O$), hexamethylene tetramine (HMT), 4-nitrophenol (4-NP), arylboronic acid, and aryl halide were bought from Sinopharm Chemical Reagent (Shanghai, China). All the reagents were of analytical grade and directly used without further purification.

Synthesis of core–shell Fe_3O_4@C nanoparticles

The magnetic Fe_3O_4 nanoparticles modified by trisodium citrate were prepared according to the study reported by Zhao.[38] Fe_3O_4@C nanoparticles were synthesized by a versatile hydrothermal method. Briefly, 1 g of as-prepared Fe_3O_4 nanoparticles and 3.24 g of glucose were dispersed in 60 mL water. After ultrasonication for 30 min, the mixture was transferred to a Teflon-lined stainless-steel autoclave (90 mL volume), and then sealed to heat at 180 °C for 4 h. The products were collected from the solution through an external magnet and washed three times with deionized water and ethanol, and then vacuum dried at 60 °C overnight.

Synthesis of core–shell Fe_3O_4@C–Pd nanoparticles

Fe_3O_4@C–Pd nanoparticles were synthesized by the deposition–precipitation method. Typically, 100 mg Fe_3O_4@C nanoparticles were dispersed in 120 mL 1 : 1 water/ethanol with ultrasonication for 30 min. Then, 5 mL 0.01 M $PdCl_2$ ethanol dispersion was added into the abovementioned solution. After ultrasound treatment for another 30 min, the obtained mixture was then mechanically stirred at 100 °C for 50 min, and then allowed to cool to room temperature. The products were separated by applying an external magnet and washed three times with deionized water and ethanol, and then vacuum dried at 60 °C overnight.

Synthesis of core–shell Fe_3O_4@C–Pd@*m*CeO_2 nanoparticles

100 mg Fe_3O_4@C–Pd nanoparticles were dispersed and sonicated for 30 min in 60 mL ethanol. 200 mg $Ce(NO_3)_3 \cdot 6H_2O$ was dissolved in 60 mL ethanol, and mixed with the above mentioned solution under an ultrasound treatment process for 10 min. Subsequently, 0.8 g HMT dissolved in 80 mL pure water was added to the mixture solution with ultrasonication for another 15 min. The mixture was then mechanically stirred for 2 h at 70 °C. The resultant products were separated with a magnet, and washed with water five times to remove any potential ionic remnants. Finally, the products were vacuum dried at 60 °C overnight. The powder was calcined at 400 °C for 2 h to obtain Fe_3O_4@C–Pd@*m*CeO_2 nanoparticles. The product was decomposed in concentrated nitric acid, and then analysed *via* an inductively coupled plasma atomic emission spectrometer (ICP-AES) to determine the content of Pd (3.05 wt%).

The synthesis process of Fe_3O_4@C@*m*CeO_2 nanoparticles was the same as that of Fe_3O_4@C–Pd@*m*CeO_2 nanoparticles without the Pd nanoparticles.

Suzuki–Miyaura cross-coupling reactions

The Fe_3O_4@C–Pd@*m*CeO_2 catalyst (10 mg), aryl halide (1.0 mmol), arylboronic acid (1.2 mmol) and potassium carbonate (2 mmol) were placed in a Schlenk tube containing a magnetic stirrer (in the case of stirring, the catalyst has good solubility in the solvent of our choice and solvent (5 mL) was then added. The mixture was stirred at 80 °C in air. The reaction process was monitored by GC at fixed time intervals. The catalyst was separated from the mixture with a magnet, washed several times with water and ethanol, and then dried in vacuum at 60 °C overnight. The recycling experiment was carried out following the same procedures.

Reduction of 4-NP

The reduction of 4-NP was tested in a quartz cuvette and monitored by UV-vis spectroscopy (Shimadzu UV-3600) at room temperature. In a typical procedure, 4.0 mg of Fe_3O_4@C–Pd@*m*CeO_2 composites were homogeneously dispersed into the 4.0 mL 4-NP solution (10 mg L^{-1}), followed by a quick injection of 1 mL of fresh $NaBH_4$ solution (10 mg mL^{-1}) under stirring. The color of the mixture solution gradually changed from yellow to colorless, indicating that the Fe_3O_4@C–Pd@*m*CeO_2 composites catalyzed the reduction of 4-NP. After stirring every ten seconds, the mixture was rapidly moved to a quartz cell to monitor the reduction progress by recording the UV-vis absorption spectra of the solution. The 4-NP has a strong absorption peak at 400 nm in the presence of $NaBH_4$, while the product of 4-aminophenol has a moderate absorption peak at 295 nm.

In the recycling study, the Fe_3O_4@C–Pd@*m*CeO_2 composites were separated from the mixture using a magnet after the reduction reaction was complete. After washing with ethanol and water three times, they were utilized in the next reaction run in a similar manner to the abovementioned reduction process.

Characterization

FT-IR was recorded over the wavenumber range from 4000 to 400 cm^{-1} on a Nicolet IS10 spectrometer, and solid samples were measured with KBr disks. XRD analyses were recorded on a D/max-γB diffractometer using Cu Kα radiation. Transmission electron microscopy (TEM) measurements were obtained on a JEOL 2010F microscope operating at 200 kV. The samples were dispersed in ethanol and transferred onto holey carbon films supported with a Cu grid for TEM measurements. High resolution transmission electron microscopy (HR-TEM) and scanning transmission electron microscopy (STEM) images were obtained on a JEM-2100F scanning transmission electron microscope to characterize the morphologies of the particles. Scanning electron microscopy (SEM) images were obtained from a Philips XL30FEG. The samples were dispersed in ethanol and transferred onto a silicon chip for SEM measurements. N_2 sorption isotherms were obtained with a Micromerits Tristar 3000 analyzer at 77 K. The powder was degassed at 200 °C in a vacuum for 10 h. Using the Barrett–Joyner–Halenda (BJH) model, the pore volumes and the pore size distributions were acquired from the adsorption branches of the isotherms. The Brunauer–Emmett–Teller (BET) method was used to count the specific surface areas using adsorption date. The magnetization curve of the sample was recorded on a superconducting quantum interference device (SQUID) magnetometer (Quantum Design MPMS XL-7) at 300 K. X-ray photoelectron spectroscopy (XPS) was collected on XR 5 VG (UK) using a monochromatic Mg X-ray source. Binding energy standardization was based on C 1s at 284.6 eV.

Results and discussion

The procedure for the preparation of hierarchical core–shell nanospheres, designated as Fe_3O_4@C–Pd@*m*CeO_2, is shown in Scheme 1. First, the Fe_3O_4 nanoparticles modified by trisodium citrate were prepared *via* a rough solvothermal reaction grounded on a high temperature reduction of $FeCl_3·6H_2O$ in the presence of EG and NaAc.[38] Then, a uniform carbon coating was fabricated on the surface of Fe_3O_4 nanoparticles through hydrothermal treatment with glucose as the carbon source, resulting in core–shell Fe_3O_4@C nanospheres. Subsequently, Pd NPs were deposited on the surface of the carbon-protected Fe_3O_4 nanospheres by refluxing in an ethanol/water solution using $PdCl_2$ as the precursor without any additional reducing agents.[22] The prepared Pd-immobilized Fe_3O_4@C nanospheres were denoted as Fe_3O_4@C–Pd. Finally, $Ce(NO_3)_3·6H_2O$ was used as a cerium source and HMT was applied to slowly produce OH^- for obtaining a homogenous CeO_2 coating surrounding the Fe_3O_4@C–Pd nanospheres through an assembly sol–gel process. Subsequently, HMT was removed by a calcination process and a porous CeO_2 shell could be obtained,[40] resulting in Fe_3O_4@C–Pd@*m*CeO_2 nanospheres with a sandwich-like structure.

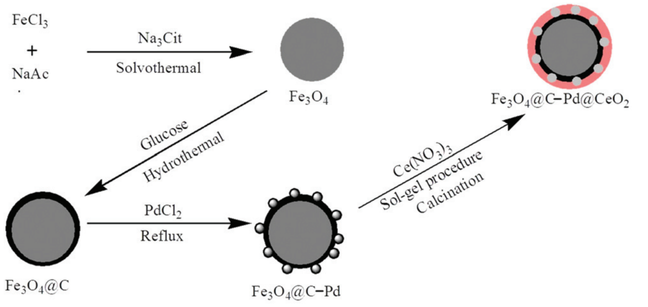

Scheme 1 Schematic of the preparation of Fe_3O_4@C–Pd@*m*CeO_2 composites.

The morphology and structure of the as-prepared composites were investigated by SEM and TEM. Fig. 1a and b show the SEM images of the Fe_3O_4@C–Pd@*m*CeO_2 nanospheres. It can be seen from the images that the Fe_3O_4@C–Pd@*m*CeO_2 nanospheres have sizes in the range of 250–300 nm with a spherical shape. Fig. S1† shows the EDX spectrum of Fe_3O_4@C–Pd@*m*CeO_2 nanospheres. The loading amount of Pd in the Fe_3O_4@C–Pd@*m*CeO_2 catalyst is estimated to be 0.35 atom% from the EDX analysis. Fig. 2a and b show the TEM images of the Fe_3O_4@C after the hydrothermal reaction of Fe_3O_4 NPs; a thin carbon layer of ~8 nm thickness was formed on the Fe_3O_4 nanospheres, resulting in core–shell Fe_3O_4@C nanospheres. After the deposition of Pd NPs, numer-

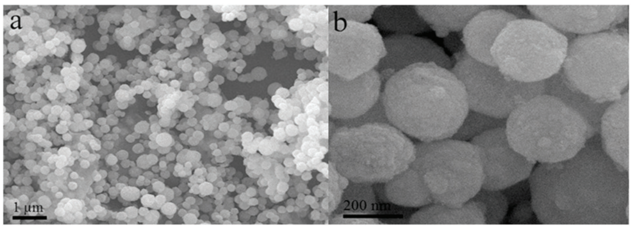

Fig. 1 SEM images of Fe_3O_4@C–Pd@*m*CeO_2 (a) 1 μm; (b) 200 nm.

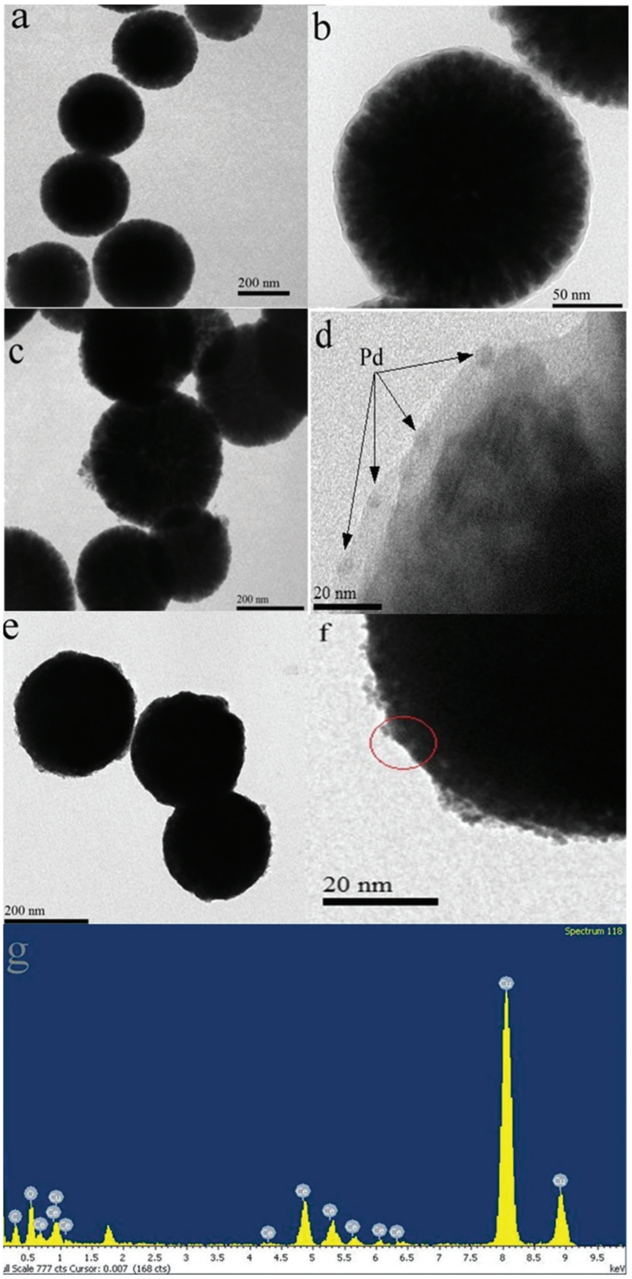

Fig. 2 TEM images of (a and b) Fe_3O_4@C nanospheres; (c and d) Fe_3O_4@C–Pd nanospheres; (e and f) Fe_3O_4@C–Pd@*m*CeO_2 nanospheres; (g) EDX corresponding to the red circular region of panel f.

ous monodispersed Pd NPs were uniformly deposited on the carbon shell with an average size of 4–5 nm, producing Fe_3O_4@C–Pd nanospheres (Fig. 2c and d). After further deposition of a homogenous CeO_2 shell, Fe_3O_4@C–Pd@*m*CeO_2 nanospheres with a regular spherical morphology were obtained (Fig. 2e and f).

However, because of the high electron density of polycrystalline CeO_2,[41] the small size of Pd NPs and the specific core–shell architecture, it is difficult to recognize the interface between Pd NPs and CeO_2. Therefore, the encapsulated Pd NPs cannot be visualized evidently from the TEM image of the Fe_3O_4@C–Pd@*m*CeO_2 nanospheres.[41] In addition, the selected areas of the red circular region of panels, shown in Fig. 2g, provides EDX results showing that the main element present in the outermost shell of the nanospheres is cerium. Therefore, the HR-TEM images shown in Fig. 3a and b further demonstrate that the relatively crude surface is composed of ultrafine Pd and CeO_2 nanocrystallites with main sizes of approximately 4.5 nm and 5 nm. The lattice fringes are obviously visible with *d*-spacings of about 0.32 nm and 0.21 nm, which readily index to the lattice spacings of (111) planes of the cubic uorite phase of CeO_2 and (111) lattice planes of Pd NPs.[42] in addition, scanning transmission electron microscopy (STEM) and EDS elemental mapping were also implemented to uncover the elemental distribution in these structured microspheres. The STEM images in Fig. 3c reveal that the structures are core–shell structured microspheres. The corresponding EDS mapping images results indicate that the Fe, Ce, O and Pd elements are dispersed evenly throughout the whole spheres. The elements Pd and Ce are thoroughly distributed in the outermost surface of the microspheres, which confirms the hierarchical core–shell structure of Fe_3O_4@C–Pd@*m*CeO_2 obtained by the elaborate assembly procedures and is illustrated in Scheme 1.

To further confirm the presence of Pd NPs and CeO_2 in the shell, surface analysis of the prepared nanospheres was carried out using XPS (Fig. 4). In Fig. 4a, it is difficult to observe the peak of iron element from the XPS spectrum of Fe_3O_4@C–Pd nanospheres, suggesting that the Fe_3O_4 nanospheres were thoroughly coated by a carbon layer to form a core–shell structure.[42] The regional XPS spectrum of Fig. 4b shows two peaks at 341.1 and 335.7 eV, which correspond to $3d_{3/2}$ and $3d_{5/2}$ of Pd(0), respectively. This indicates that the Pd(0) NPs were

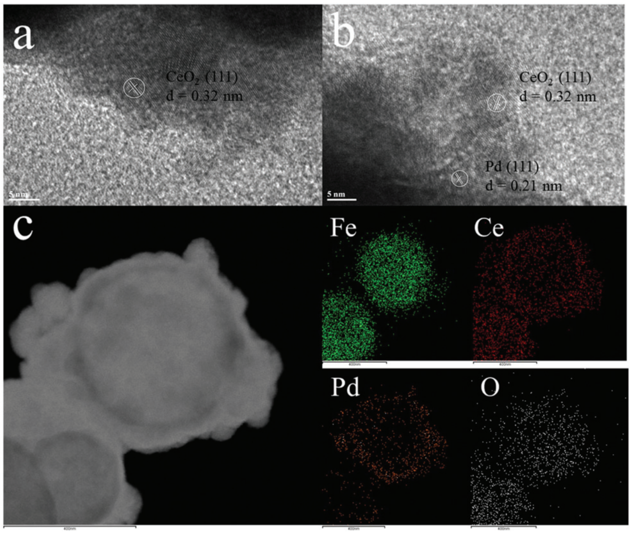

Fig. 3 (a and b) HR-TEM images of Fe_3O_4@C–Pd@*m*CeO_2 nanospheres, (c) HADDF-STEM images of Fe_3O_4@C–Pd@*m*CeO_2 nanospheres and corresponding EDS mapping images.

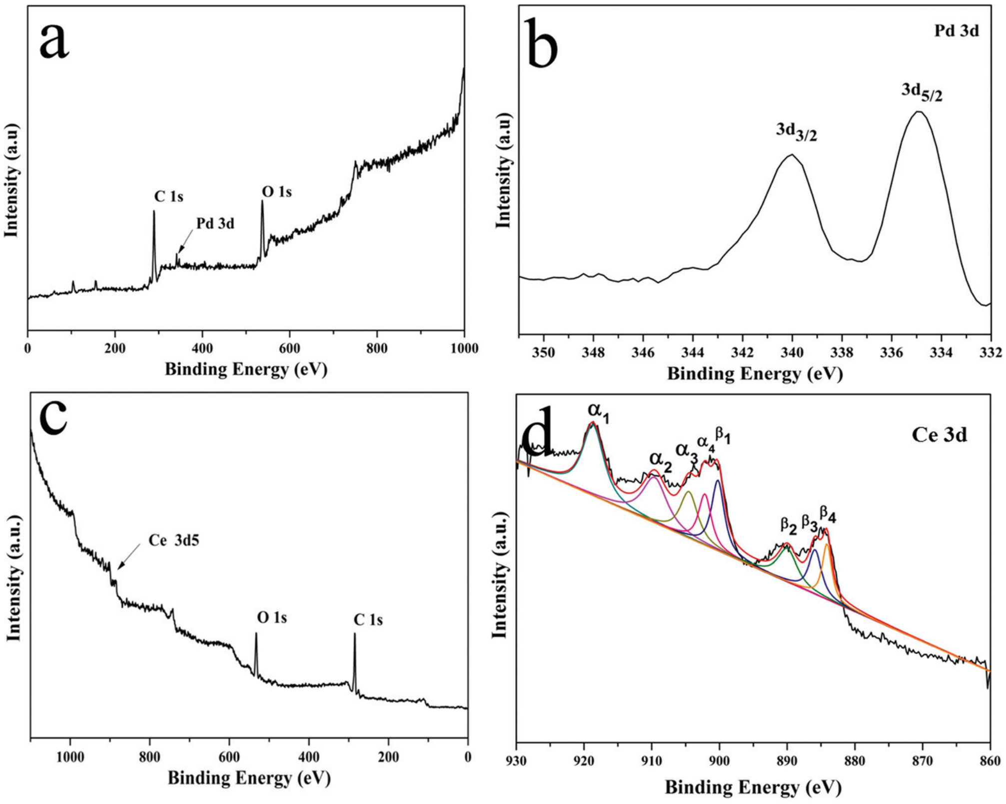

Fig. 4 XPS spectra of (a) Fe_3O_4@C–Pd nanospheres and (b) Pd 3d; (c) Fe_3O_4@C–Pd@*m*CeO_2 nanospheres and (d) Ce 3d.

formed on the surface of the Fe_3O_4@C nanospheres.[42] The XPS spectrum of Fe_3O_4@C–Pd@*m*CeO_2 nanospheres (Fig. 4c) reveals that carbon, oxygen and cerium are present on the surface of the nanospheres. Concerning the characteristic signals of the Ce3d spectrum, the four primary $3d_{3/2}$ peaks were located around 917.8 eV, 907.8 eV, 904.5 eV and 901.6 eV, matching the α_1, α_2, α_3 and α_4 components, respectively, whereas the $Ce3d_{5/2}$ peaks were located around 898.7 eV, 888.0 eV, 885.3 eV, and 883.0 eV in accordance with β_1, β_2, β_3 and β_4, respectively (Fig. 4d).[43] Both the signals α_3 and β_3 are the characteristic peaks of Ce^{3+}, while the other peaks correspond to the characteristic peaks of Ce^{4+}. The presence of Ce^{3+} can be conducive to the synergistic effect between the CeO_2 nanoparticles and noble metal NPs.[44] The $Ce^{3+}:Ce^{4+}$ ratio in the Fe_3O_4@C–Pd@*m*CeO_2 catalyst was *ca.* 18%.

Fig. S2† shows the FT-IR spectra of Fe_3O_4 nanospheres, core–shell Fe_3O_4@C nanospheres, Fe_3O_4@C–Pd nanospheres and Fe_3O_4@C–Pd@*m*CeO_2 nanospheres synthesized in this study. The FT-IR spectrum of magnetite nanoparticles (Fig. S2a†) shows absorption bands at 583 and 1650 cm^{-1}, which are attributed to the vibration mode of Fe–O and the carbonyl group of trisodium citrate.[45] The bands around 3400 cm^{-1} are ascribed to the OH vibration. From Fig. S1b,† for core–shell Fe_3O_4@C nanoparticles, the peaks around 1620 cm^{-1} are related to the aromatization of glucose during hydrothermal treatment.[46] From Fig. S2c and S2d,† the absorption peaks of Fe_3O_4@C–Pd nanospheres and Fe_3O_4@C–Pd@*m*CeO_2 nanospheres are similar to those of the Fe_3O_4@C nanospheres. However, it is noteworthy that the intensity of absorption peaks was significantly weaker than that of Fe_3O_4@C nanoparticles after being anchored with Pd nanoparticles and coated by CeO_2.

The phase and composition of the resulting products are profoundly characterized by XRD in Fig. 5. In Fig. 5a, all the peaks at about 29.9°, 35.3°, 43.0°, 56.9° and 62.5° are associated with Fe_3O_4 (220), (311), (440), (511) and (220) peaks of a face centered cubic. According to Fig. 5b, there is no obvious change in the XRD of the Fe_3O_4@C nanospheres compared with that of the Fe_3O_4 nanospheres. The XRD pattern of Fe_3O_4@C–Pd is shown in Fig. 5c; addition the peaks of Fe_3O_4 core, additional peaks are located near 40.0°, which are well-indexed to face centered Pd (111) peaks (JCPDS no. 05-0681).[42] Fig. 5d and e show the XRD patterns of Fe_3O_4@C@*m*CeO_2 nanoparticles and core–shell Fe_3O_4@C–Pd@*m*CeO_2 nanoparticles; both the figures exhibit peaks at 28.7°, 33.2°, 47.8°, and 56.3°, corresponding to the (111), (200), (220), and (311) Bragg diffraction of CeO_2 (JCPDS no. 34-0394).[39] There are no diffraction peaks matching to those of Pd nanoparticles in the Fig. 5e owing to their high dispersity and the low content loading.[42]

The magnetic performances of the samples were investigated using a SQUID magnetometer at 300 K from −20 000 to

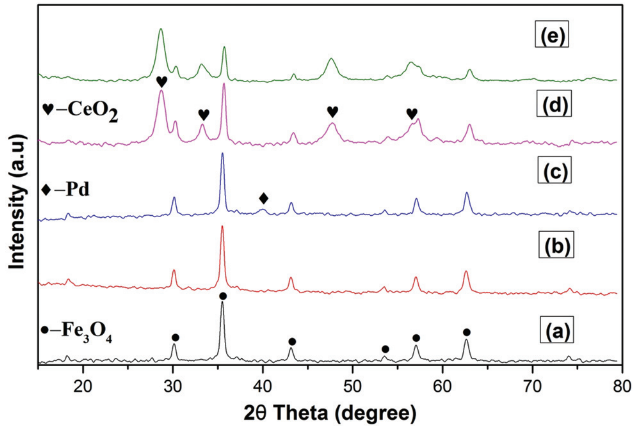

Fig. 5 XRD pattern of (a) Fe_3O_4 nanospheres, (b) Fe_3O_4@C nanospheres, (c) Fe_3O_4@C–Pd nanospheres, (d) Fe_3O_4@C@*m*CeO_2 nanospheres and (e) Fe_3O_4@C–Pd@*m*CeO_2 nanospheres.

20 000 Oe. Fig. S3† shows the magnetization curves of Fe_3O_4 nanospheres (black), Fe_3O_4@C nanospheres (red), Fe_3O_4@C–Pd nanospheres (blue) and Fe_3O_4@C–Pd@*m*CeO_2 nanoparticles (pink). At 300 K, the saturation magnetization value is 74.9, 25.5, 24.6 and 21.3 emu per g, respectively. The inset in Fig. S3† shows the photograph of the dispersion of 5 mg mL^{-1} Fe_3O_4@C–Pd@*m*CeO_2 nanospheres in water before and after magnetic separation. To further analyse the pore size distribution, BET measurements were carried out. As shown in Fig. 6, the N_2 adsorption–desorption isotherms of the Fe_3O_4@C–Pd@*m*CeO_2 composites exhibit representative type-IV curves, and the BET surface area is about 85 m^2 g^{-1}. The pore size distribution shows that the pores size mostly range from 2.0 to 4.5 nm with an intense peak appearing at around 3.5 nm, indicating a mesoporous CeO_2 shell. This result is in good agreement with the literature.[40]

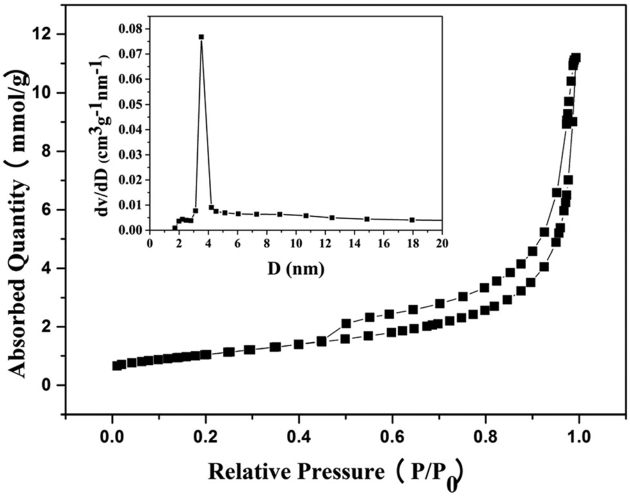

Fig. 6 Nitrogen adsorption–desorption isotherm plots of Fe_3O_4@C–Pd@*m*CeO_2 and pore size distribution curves of Fe_3O_4@C–Pd@*m*CeO_2 (inset).

The successful synthesis of Fe_3O_4@C–Pd@*m*CeO_2 nanospheres can be attributed to the following outlines. First, the Fe_3O_4 nanoparticles synthesized by the solvothermal reaction are modified by citrate groups. Therefore, they can be highly dispersible in water and ethanol, favouring the further coating with other oxides or polymers.[45] Thus, a thin carbon layer can be readily coated onto the Fe_3O_4 nanoparticles by the partial carbonization and polymerization of glucose under hydrothermal treatment.[46] Second, the existence of reductive groups (such as –OH and –CHO) in the carbon shell, appeared due to the dehydration of the glucose, can facilitate *in situ* reduction of $PdCl_2$. Therefore, no additional reducing or linker agents are needed.[22] Third, because the obtained Fe_3O_4@C–Pd nanospheres are hydrophilic and have good dispersibility in ethanol and water, the subsequent surface coating of the mesoporous CeO_2 can be achieved.

Based on the high dispersibility, we evaluated the catalytic efficiency for the Suzuki–Miyaura reaction (cross-coupling of 4-iodoanisole and phenylboronic acid) in a green medium of water or ethanol without any external promoters, phosphine ligands or biphasic media. From the results in Table S1,† we can see that a low-grade yield of the desired resultant was obtained by the Fe_3O_4@C@*m*CeO_2 without Pd NPs in an ethanol solvent (Table S1,† entry 1). No obvious increase in yield was observed by increasing the reaction time (Table S1,† entry 2). This suggests that ceria has a catalytic effect for the Suzuki–Miyaura reaction.[47] With water as the solvent, the reaction did not occur at all (Table S1,† entry 3). Significantly, the model reaction using Fe_3O_4@C–Pd or Fe_3O_4@C–Pd@*m*CeO_2 as the catalyst in water or ethanol or their mixture at 80 °C afforded the desired product within 3 h in excellent isolated yield (Table S1,† entries 4–9). Interestingly, other solvents, such as isopropanol, tetrahydrofuran, *N*,*N*-dimethylformamide, 1,4-dioxane, dimethyl sulfoxide, dimethylacetamide, toluene and dimethylbenzene, supported the same catalytic reaction of Fe_3O_4@C–Pd@*m*CeO_2 fairly well (Table S2,† entries 1–8).

To explore the expansion of this reaction, a series of aryl iodides were selected to react with phenylboronic acid with a mixed solvent of ethanol/water (1 : 1) and K_2CO_3. It is worth noting that Fe_3O_4@C–Pd@*m*CeO_2 as the catalyst can tolerate a wider range of functional groups (Table 1, entries 2–7) such as –Me, $–OCH_2CH_3$, $–OCF_3$, –OH, $–NH_2$ and $–COCH_3$. Interestingly, aryl bromides delivered the products with high yields under identical conditions (Table 1, entries 8–9). However, aryl chloride is relatively troublesome for the same process providing a medium yield (Table 1, entries 10–11). An array of substituted arylboronic acid substrates also underwent the cross-coupling reaction with aryl halide with our catalytic system (Table 1, entries 13–30). *Ortho*-methyl phenylboronic acid gave good yields of the 2-arylation product (Table 1, entries 13, 18, 23, and 27), which was not impaired by steric hindrance. A satisfactory yield was also obtained by 1-naphthylboronic acid for the formation of 1-arylation naphthalane (Table 1, entries 16,

Table 1 The Suzuki reactions catalyzed by Fe_3O_4@C–Pd@*m*CeO_2 catalyst[a]

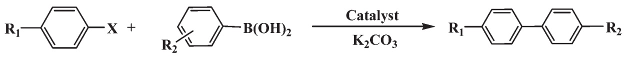

Entry	R_1	X	R_2	Yield[b]	TOF[d]
1	H	I	H	>99[c]	345.4
2	OCF_3	I	H	93	108.2
3	OH	I	H	95	116.3
4	OCH_2CH_3	I	H	92	107.0
5	NH_2	I	H	95	116.3
6	CH_3	I	H	95	116.3
7	COCH3	I	H	90	104.6
8	H	Br	H	95	116.3
9	CH_3	Br	H	90	104.6
10	H	Cl	H	50	58.2
11	CH_3	Cl	H	58	67.5
12	OCH_3	I	H	99	115.1
13	OCH_3	I	2-CH_3	90	104.6
14	OCH_3	I	4-CH_3	95	116.3
15	OCH_3	I	4-F	98	113.9
16	OCH_3	I	1-Naphthyl	85	98.9
17	$COCH_3$	I	4-OCH_3	82	95.4
18	$COCH_3$	I	2-CH_3	75	88.4
19	$COCH_3$	I	4-CH_3	88	102.3
20	$COCH_3$	I	4-F	93	108.2
21	$COCH_3$	I	1-Naphthyl	73	84.9
22	H	Br	4-OCH_3	88	102.3
23	H	Br	2-CH_3	68	79.1
24	H	Br	4-CH_3	78	90.7
25	H	Br	4-F	85	98.9
26	H	Br	1-Naphthyl	72	83.7
27	CH_3	Br	2-CH_3	75	88.4
28	CH_3	Br	4-OCH_3	85	98.9
29	CH_3	Br	4-F	86	100.0
30	CH_3	Br	1-Naphthyl	77	90.7

[a] Reaction conditions: aryl halide (1.0 mmol), arylboronic acid (1.2 mmol), potassium carbonate (2 mmol), 5 mL ethanol–water (1 : 1), 10 mg Fe_3O_4@C–Pd@*m*CeO_2 (Pd 3.05 wt%) at 80 °C for 3 h. [b] Isolated yields. [c] 60 °C for 45 min. [d] TOF was defined as mol product mol^{-1} Pd h^{-1}.

21, 26, and 30). Both electron-withdrawing (4-F) and electron-donating (4-OCH_3) groups did not show an inhibition effect under the same conditions (Table 1, entries 15, 17, 20, 25, 28, and 29).

We further compared the catalytic results obtained with this hierarchical "shell-in-shell" structure with other traditional supported Pd-based catalysts such as mesoporous carbon, polymer, silica or oxide. With the reaction of iodobenzene and phenylboronic acid as an example, the results are listed in Table S4.† It can be clearly seen that the results achieved in this study are superior to others. Even though some of these materials also can acquire high yield, toxic solvents (such as DMF, CH_2Cl_2, or THF) or a long time were required. These solvent are less favorable compared to the ethanol–water mixture used in this study. The comparison of the catalytic performance between the catalyst of Fe_3O_4@C–Pd@*m*SiO_2[22] and our Fe_3O_4@C–Pd@*m*CeO_2 system has also been summarized in Table S5.† It can be clearly observed that the catalytic performance of our Fe_3O_4@C–Pd@*m*CeO_2 system is better than that of the catalyst of Fe_3O_4@C–Pd@*m*SiO_2.

The catalytic property of the Fe_3O_4@C–Pd@*m*CeO_2 composites was also evaluated by the reduction of 4-NP to 4-aminophenol (4-AP) in the presence of $NaBH_4$, which is one of the representative model reactions for estimating the catalytic activity of the noble metal NPs.[42] As shown in Fig. 7a, when a trace amount of the Fe_3O_4@C–Pd@*m*CeO_2 nanocatalyst (2 mg) is introduced into the solution, the absorption peak at 400 nm decreases in a certain period of time and, simultaneously, a new absorption peak at 295 nm arises, which can be attributed to the reduction of 4-NP and the emergence of 4-AP, respectively. For comparison, the catalytic activities of Fe_3O_4@C@*m*CeO_2 and Fe_3O_4@C–Pd as reference catalysts have also been investigated following the identical experimental conditions. The conversion can be directly determined from the curves made of the percentage of the absorbance intensity of 4-NP at an interval time to its initial absorbance intensity value, as displayed in Fig. 7b. It is obvious that Fe_3O_4@C@*m*CeO_2 exhibits negligible catalytic reduction activity, suggesting that the reduction reaction is mainly catalyzed by the Pd NPs, whereas

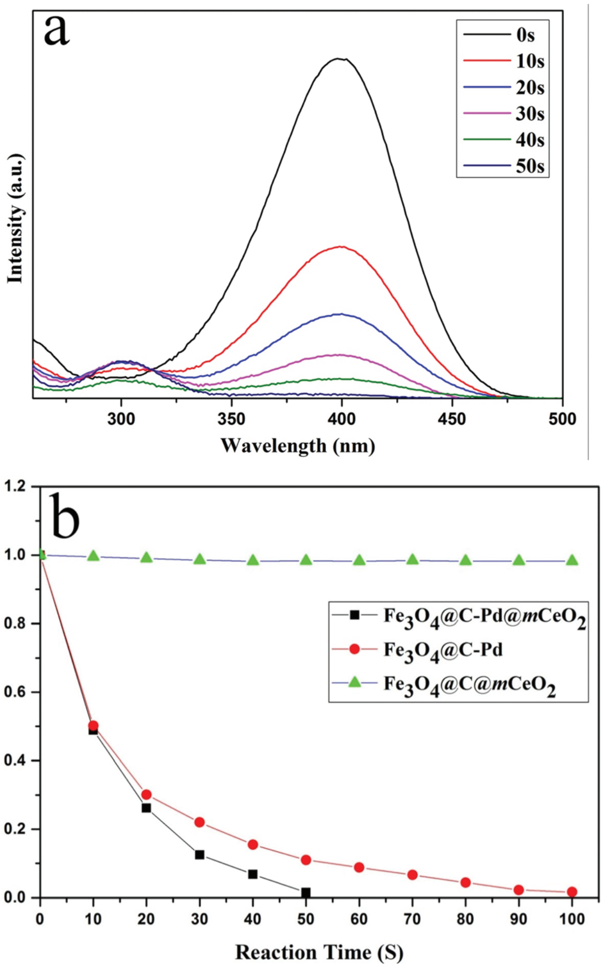

Fig. 7 (a) UV-vis spectra of 4-NP and $NaBH_4$ solution in the presence of 2 mg Fe_3O_4@C–Pd@*m*CeO_2; (b) Performance of Fe_3O_4@C–Pd@*m*CeO_2, Fe_3O_4@C–Pd, and Fe_3O_4@C@*m*CeO_2 nanocomposites for the reduction of 4-NP.

the supported Fe_3O_4@C–Pd possesses inferior catalytic performance as compared to Fe_3O_4@C–Pd@*m*CeO_2 nanocomposites.

In addition to the outstanding catalytic activity, isolation and reusability of the catalyst is a considerable requirement for any practical application in accordance with budget and environmental protection,[48–50] are the greatest merits in our study. In our systems, the catalysts can be easily retrieved using an external magnet, as proved shown in Fig. S3† inset. In order to investigate the reusability of the catalyst, both the Suzuki–Miyaura reaction (cross-coupling of 4-iodoanisole and phenylboronic acid) and the reduction of 4-NP were chosen. As illustrated in Fig. S4a and S4b,† the catalyst Fe_3O_4@C–Pd@*m*CeO_2 can be reused ten times without an obvious decrease in conversion and selectivity for both the reactions by a simple magnetic separation. However, the results of Fig. S4c and S4d† reveal that the catalytic activity of the Fe_3O_4@C–Pd was found to distinctly decrease during the recycling test after the two reduction process were repeated four times. Fig. S5† shows the TEM images of Fe_3O_4@C–Pd@*m*CeO_2 after 10 runs of recycling experiments for the Suzuki reactions. The images indicate that the catalyst still maintained a spherical shape after the recycling experiments.

Based on the abovementioned data, it could be readily concluded that the catalytic activity of Fe_3O_4@C–Pd@*m*CeO_2 is better than that of Fe_3O_4@C–Pd for the two reactions, and it can be easily deduced that the Fe_3O_4@C–Pd@*m*CeO_2 core–shell nanostructure can effectively block the aggregation of the Pd NPs due to the robust protection of CeO_2 shells, thereby holding the high catalytic property of the Pd NPs. The other more remarkable advantage of Fe_3O_4@C–Pd@*m*CeO_2 as a distinct compared to Fe_3O_4@C–Pd for mediating these reactions in solution is that the CeO_2 shells can effectively hinder the leaching of Pd NPs. The leaching test of Pd was analysed by ICP-AES after ten cycles, and the results are listed in Table S3.† Both reactions show determinable Pd loss; the trace content of Pd loss indicates that Fe_3O_4@C–Pd@*m*CeO_2 can be a reusable catalyst with additional anti-deactivation performance. This prominent characteristic can be confirmed by the very steady recycling catalytic activity test on Fe_3O_4@C–Pd@*m*CeO_2 (Fig. S4a and S4b†) and its steady nanostructure.

Over the past few decades, the comprehending of the interfacial effect between the noble metal NPs and the metal oxide supports is still ambiguous for heterogeneous reactions because multiple factors influence the catalytic activity of Pd nanocatalysts.[51,52] Many metal oxides have been employed as catalyst supports for the loading of the noble metal NPs to boost their catalytic activity and stability. CeO_2, which has a Ce^{4+}/Ce^{3+} redox cycle, is an ideal carrier due to its high oxygen storage capability, high oxygen mobility and low cost.[53,54] CeO_2 belongs to the fluorite structure, in which each O^{2-} anion is encircled by a tetrahedron of Ce^{4+} cations situated at the center of a cubic array of equivalent O^{2-} atoms.[55] However, the non-stoichiometric oxides CeO_{2-x}, which were obtained through the wet-chemical synthesis, have a high density of oxygen vacancies. The partial elimination of O atoms from O^{2-} in the CeO_2 structure can form O vacancy. The surplus electrons may either thoroughly delocalize in the conductor band, or distribute among a few Ce^{3+} cations to surround the O vacancies, or localize on the Ce^{4+} to form tetravalent Ce.[56] Ce^{3+} is an electron-rich species and tends to afford electrons to metal catalysts.[57] Simultaneously, water dissociation occurring at the O vacancy can produce the reactive OH groups.[58] Both the Ce^{3+} species and OH groups are reactive δ^- sites, which can endow electrons to Pd NPs. Therefore, the Ce^{3+} fraction and O-vacancy concentration can be used to comprehend the synergistically catalytic effect for enhancing the catalytic activity.

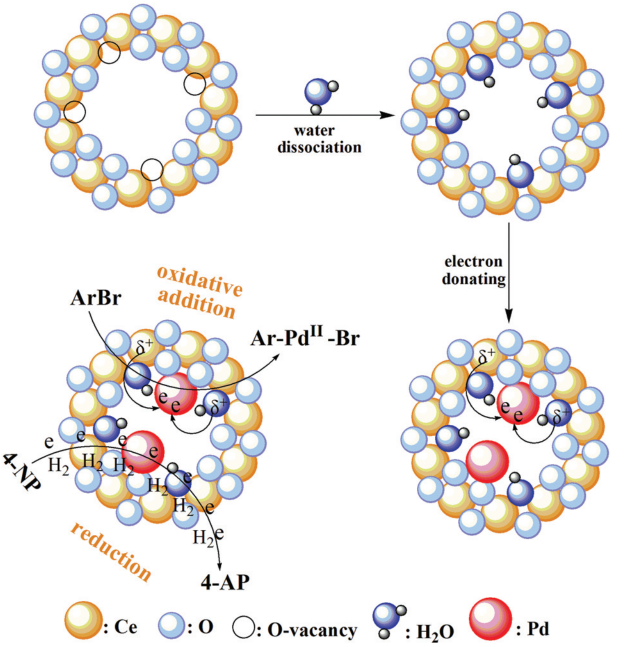

Scheme 2 The proposed mechanism for the synergistic effect between the CeO_2 NPs and Pd NPs with improved catalytic activity.

A proposed reaction mechanism for the synergistically catalytic effect is illustrated in Scheme 2. During the wet-chemical synthesis process of the CeO_2, the Ce^{3+} cationic species (which was also confirmed by XPS in Fig. 3d) and O vacancies are formed. The active OH groups will be produced through the dissociation of water on the O-vacancy sites.[59] Afterwards, the electron pair donors of the Ce^{3+} cationic species and OH groups can be transferred to the Pd NPs *via* the electron-donating effect, leading to a higher electron density Pd NPs. This serves to improve the first step of the oxidative addition reaction, formation of the radical ligand Ar–Pd^{II}–Br. This step is regarded as the key step in the C–C coupling reactions.[52] The high density of electron of Pd NPs also can rapidly catalyze the reduction of 4-NP.

Conclusions

In summary, we demonstrate a successful preparation of multicomponent and multifunctional Fe_3O_4@C–Pd@CeO_2

nanospheres with well-defined magnetic core–shell nanostructures, confined catalytic Pd NPs and accessible mesoporous CeO_2 by combining the hydrothermal method, interfacial *in situ* deposition and a sol–gel process. The well-designed hierarchical nanospheres have high magnetization (21.3 emu per g), with a highly open mesoporous characteristics (~3.5 nm in diameter), and smoothly restricted but uncovered catalytic Pd NPs that uniformly disperse between the carbon-protected Fe_3O_4 core and the mesoporous CeO_2 shell. The as-obtained multifunctional Fe_3O_4@C–Pd@CeO_2 nanospheres show excellent catalytic performance in the Suzuki–Miyaura cross-coupling reaction and the reduction of 4-nitrophenol both with convenient separability and remarkable reusability without loss activity after reusing ten times. Therefore, as a novel Pd-based catalyst system, this multifunctional core–shell nanostructure holds great promise for various catalytic reactions. In addition, the design idea for the hierarchical nanomaterials can be expanded to the synthesis of other multicomponent nanomaterials with integrated and enhanced capabilities for various applications.

References

1 G. V. Hartland, *Chem. Rev.*, 2011, **111**, 3858–3887.
2 S. N. Tian, Z. Zhou, S. Sun, Y. Ding and Z. L. Wang, *Science*, 2007, **316**, 732–735.
3 T. K. Sau, A. L. Rogach, F. Jäckel, T. A. Klar and J. Feldmann, *Adv. Mater.*, 2010, **22**, 1805–1825.
4 S. Linic, P. Christopher and D. B. Ingram, *Nat. Mater.*, 2011, **10**, 911–921.
5 A. Scholl and A. Dionne, *Nature*, 2012, **483**, 421–427.
6 L. Chen, G. Chen, C. Leung, S. Yiu, C. Ko, E. Anxolabéhère-Mallart, M. Robert and T. Lau, *ACS Catal.*, 2015, **5**, 356–364.
7 L. Zhong, A. Chokkalingam, W. S. Cha, K. S. Lakhi, X. Su, G. Lawrence and A. Vinu, *Catal. Today*, 2015, **243**, 195–198.
8 A. Sanchez, S. Abbet, U. Heiz, W. D. Schneider, H. Häkkinen, R. N. Barnett and U. Landman, *J. Phys. Chem. A*, 1999, **103**, 9573–9578.
9 E. Yoo, T. Okata, T. Akita, M. Kohyama, J. Nakamura and I. Honma, *Nano Lett.*, 2009, **9**, 2255–2259.
10 C. An, S. Peng and Y. Sun, *Adv. Mater.*, 2010, **22**, 2570–2574.
11 K. Soukup, P. Topka, V. Hejtmánek, D. Petráš, V. Valeš and O. Šolcová, *Catal. Today*, 2014, **236**, 3–11.
12 R. G. Chaudhuri and S. Paria, *Chem. Rev.*, 2012, **112**, 2373–2433.
13 J. M. Thomas, B. F. G. Johnson, R. Raja, G. Sankar and P. A. Midgley, *Acc. Chem. Res.*, 2003, **36**, 20–30.
14 M. Liu, R. Z. Zhang and W. Chen, *Chem. Rev.*, 2014, **114**, 5117–5160.
15 Y. Zhou, H. Wang, M. Gong, Z. Sun, K. Cheng, X. Kong, Z. Guo and Q. Chen, *Dalton Trans.*, 2013, **42**, 9906–9913.
16 M. B. Gawande, R. Zboril, V. Malgras and Y. Yamauchi, *J. Mater. Chem. A*, 2015, **3**, 8241–8245.
17 M. B. Gawande, P. S. Branco and R. S. Varma, *Chem. Soc. Rev.*, 2013, **42**, 3371–3393.
18 S. Sá, M. B. Gawande, A. Velhinho, J. P. Veiga, N. Bundaleski, J. Trigueiro, A. Tolstogouzov, O. M. N. D. Teodoro, R. Zboril, R. S. Varma and P. S. Branco, *Green Chem.*, 2014, **16**, 3494–3500.
19 M. B. Gawande, R. Luque and R. Zboril, *ChemCatChem*, 2014, **6**, 3312–3313.
20 D. Wang, *Astruc. Chem. Rev.*, 2014, **114**, 6949–6985.
21 H. Hildebrand, K. Mackenzie and F. D. Kopinke, *Environ. Sci. Technol.*, 2009, **43**, 3254–3259.
22 Z. Sun, J. Yang, J. Wang, W. Li, S. Kaliaguine, X. Hou, Y. Deng and D. Zhao, *J. Mater. Chem. A*, 2014, **2**, 6071–6074.
23 Q. M. Kainz and O. Reiser, *Acc. Chem. Res.*, 2014, **47**, 667–677.
24 X. Le, Z. Dong, Y. Liu, Z. Jin, T. Huy, M. Le and J. Ma, *J. Mater. Chem. A*, 2014, **2**, 19696–19706.
25 X. X. Han, A. M. Schmidt, G. Marten, A. Fischer, I. M. Weidinger and P. Hildebrandt, *ACS Nano*, 2013, **7**, 3212–3220.
26 J. Cao, J. C. Li, L. Liu, A. J. Xie, S. K. Li, L. G. Qiu, Y. P. Yuan and Y. H. Shen, *J. Mater. Chem. A*, 2014, **2**, 7593–7597.
27 Z. J. Wu, C. G. Sun, Y. Chai and M. G. Zhang, *RSC Adv.*, 2011, **1**, 1179–1182.
28 X. B. Zhang, H. W. Tong, S. M. Liu, G. P. Yong and Y. F. Guan, *J. Mater. Chem. A*, 2013, **1**, 7488–7494.
29 Q. M. Kainz, R. Linhardt, R. N. Grass, G. Vilé, W. J. Stark and O. Reiser, *Adv. Funct. Mater.*, 2014, **24**, 2020–2027.
30 M. B. Gawande, Y. Monga, R. Zboril and R. K. Sharma, *Coord. Chem. Rev.*, 2015, **288**, 118–143.
31 R. Li, P. Zhang, Y. Huang, P. Zhang, H. Zhong and Q. Chen, *J. Mater. Chem. A*, 2012, **22**, 2275–22755.
32 T. Yao, T. Cui, J. Wu, Q. Chen, X. Yin, F. Cui and K. Sun, *Carbon*, 2012, **50**, 2287–2295.
33 T. Zeng, X. Zhang, S. Wang, Y. Ma, H. Niu and Y. Cai, *Chem – Eur. J.*, 2014, **20**, 6474–6481.
34 O. O. Fashedemi, H. A. Miller, A. Marchionni, F. Vizza and K. I. Ozoemena, *J. Mater. Chem. A*, 2015, **3**, 7145–7156.
35 M. Shokouhimehr, T. Kim, S. W. Jun, K. Shin, Y. Jang, B. H. Kim, J. Kim and T. Hyeon, *Appl. Catal., A*, 2014, **476**, 133–139.
36 B. Liu, Q. Wang, S. Yu, T. Zhao, J. Han, P. Jing, W. Hu, L. Liu, J. Zhang, L. Sun and C. Yan, *Nanoscale*, 2013, **5**, 9747–9757.
37 B. Liu, Y. Niu, Y. Li, F. Yang, J. Guo, Q. Wang, P. Jing, J. Zhang and G. Yun, *Chem. Commun.*, 2014, **50**, 12356–12359.
38 Y. Deng, Y. Cai, Z. Sun, J. Liu, C. Liu, J. Wei, W. Li, C. Liu, Y. Wang and D. Zhao, *J. Am. Chem. Soc.*, 2010, **132**, 8466–8473.
39 X. Li, X. Wang, D. Liu, S. Song and H. Zhang, *Chem. Commun.*, 2014, **50**, 7198–7201.
40 G. Cheng, J. Zhang, Y. Liu, D. Sun and J. Ni, *Chem. Commun.*, 2011, **47**, 5732–5734.
41 S. Zhang, J. Li, W. Gao and Y. Qu, *Nanoscale*, 2015, **7**, 3016–3021.
42 T. J. Yao, T. Y. Cui, X. Fang and J. Wu, *Nanoscale*, 2013, **5**, 5896–5904.

43 F. Lin, D. T. Hoang, C. K. Tsuang, W. Y. Huang and P. D. Yang, *Nano Res.*, 2011, **4**, 61–71.

44 Q. Wang, W. J. Jia, B. C. Liu, X. Gong, C. Y. Li, P. Jing, Y. J. Li, G. R. Xu and J. Zhang, *J. Mater. Chem. A*, 2013, **1**, 12732–12741.

45 J. Liu, Z. K. Sun, Y. H. Deng, Y. Zou, C. Y. Li, X. H. Guo, L. Q. Xiong, Y. Gao, F. Y. Li and D. Y. Zhao, *Angew. Chem., Int. Ed.*, 2009, **48**, 5875–5879.

46 M. Y. Zhou and G. W. Diao, *J. Phys. Chem. C*, 2011, **115**, 24743–24749.

47 A. S. Diez, M. G. Mayer and M. A. Volpe, *Appl. Catal. A*, 2014, **482**, 24–30.

48 V. Polshettiwar, R. Luque, A. Fihri, H. B. Zhu, M. Bouhrara and J. M. Basset, *Chem. Rev.*, 2011, **111**, 3036–3075.

49 J. Liu, S. Z. Qiao, Q. H. Hu and G. Q. Lu, *Small*, 2011, **4**, 425–443.

50 Y. H. Deng, Y. Cai, Z. K. Sun and D. Y. Zhao, *Chem. Phys. Lett.*, 2011, **510**, 1–13.

51 G. Chen, Y. Zhao, G. Fu, P. N. Duchesen, L. Gu, Y. Zheng, X. Weng, M. Chen, P. Zhang, C. W. Pao and N. F. Zhen, *Science*, 2014, **344**, 495–499.

52 J. Shi, *Chem. Rev.*, 2012, **113**, 2139–2181.

53 S. Tsunekawa, K. Ishikawa, Z.-Q. Li, Y. Kawazoe and A. Kasuya, *Phys. Rev. Lett.*, 2000, **85**, 3440–3443.

54 Y. Y. Chu, Z. B. Wang, Z. Z. Jiang, D. M. Gu and G. P. Yin, *Adv. Mater.*, 2011, **23**, 3100–3104.

55 Q. Wang, Y. J. Li, B. C. Liu, Q. Dong, G. R. Xu and L. Zhang, *J. Mater. Chem. A*, 2015, **3**, 139–147.

56 M. F. Camellone and S. Fabris, *J. Am. Chem. Soc.*, 2009, **131**, 10473–10483.

57 H. Y. Kim, H. M. Lee and G. Henkelman, *J. Am. Chem. Soc.*, 2012, **134**, 1560–1570.

58 Y. G. Wang, D. Mei, J. Li and R. Rousseau, *J. Phys. Chem. C*, 2013, **117**, 23082–23089.

59 Y. Wang, F. Wang, Q. Song, Q. Xin, S. Xu and J. Xu, *J. Am. Chem. Soc.*, 2013, **135**, 1506–1515.